Comparison of Three-Phase and Six-Phase High-Power Ultra-High-Speed Machine for Portable Mechanical Antenna

Md Khurshedul Islam[1], Kazi Nishat Tasnim[1], Seungdeog Choi[1], Prashant Singh[2]
Department of Electrical and Computer Engineering[1], Department of Mechanical Engineering[2]
Mississippi State University
Starkville, Mississippi 39762, USA
mi264@msstate.edu, kt1446@msstate.edu, singh@me.msstate.edu.edu, seungdeog@ece.msstate.edu

2022 IEEE Applied Power Electronics Conference and Exposition (APEC) | 978-1-6654-0688-8/22/$31.00 ©2022 IEEE | DOI: 10.1109/APEC43599.2022.9773684

***Abstract*— One of the emerging applications of the ultra-high-speed machine (UHSM) is a mechanical-based antenna (AMEBA) for portable wireless communication in the RF-denied environment. With higher power density, efficiency, and lower torque pulsation, the multi-phase UHSM can be a better substitute compared to the conventional three-phase UHSM in the AMEBA application, where portability and efficiency are the top priority. This paper presents the comparison of the three-phase and six-phase UHSM in terms of the design and performance characteristics, considering their use in a safety-critical AMEBA application. For a fair comparison, both models are designed using the same multi-physics design process. The models are optimized to maximize the efficiency, power-density, and design-safety-margin with multi-disciplinary constraints of the AMEBA system. Both models' key performances, such as the torque profile, efficiency map, back-electromotive force (EMF), temperature distribution, and developed stress, are compared by intensive simulation using finite element analysis (FEA). Finally, the optimized three-phase and six-phase UHSM prototypes (2 kW rated shaft power at 500 000 r/min) are fabricated with the same volume and same rotor geometry to validate the simulation results.**

Keywords—finite element analysis (FEA), mechanical-based antenna, Multiphysics analysis, permanent magnet machine, six-phase machine, and Ultra high speed machine.

I. Introduction

In recent years, ultra-high-speed machines (UHSM) have been developed for many emerging applications such as milling spindles, portable chargers, robotics, medicine, and rotating mirrors in the optical system [1]-[3]. Apart from these, one of the new promising applications of UHSM is a mechanical-based antenna (AMEBA), used for wireless communication in underwater or undersea facilities such as submarines, mines, tunnels, etc. [4]-[6]. Fig. 1 shows a simplified diagram of the AMEBA system using a UHSM. Unlike conventional electrical coil antenna, AMEBA uses a UHSM to rotate a polarized permanent magnet (PPM) for generating low frequency (ELF to VLF: 3 Hz to 10 kHz) electromagnetic waves that can penetrate a long distance in the RF-denied environment. Therefore, it enables portable and bidirectional communication between the earth's surface and underground or undersea facilities by solving the traditional coil antenna's excessive current and gigantic size problem. However, the critical challenge in the AMEBA development is the design of its mechanical transmitter, i.e., the UHSM, because it requires a high shaft torque at UHS to rotate the high mass density PPM dipole at a fast dynamic.

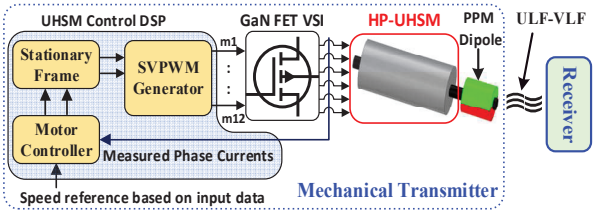

Fig. 1. Simplified AMEBA system using a high power UHSM to drive PPM.

In literature, UHSMs have been designed for different high-tech applications from 100 000 r/min to 1.2 million r/min [7], [8]. But, none of these machines are suitable for AMEBA application because they have either very low shaft torque at UHS or a large footprint that does not favor portability. On the other hand, the key requirements of an AMEBA motor are the high shaft torque at UHS, high power density, no critical bending frequency below fundamental and high efficiency with a good design safety margin (DSM).

According to the scaling law [9], the rated shaft power of the UHSM can be increased by increasing the rotor's magnetic loading. However, unlike the conventional UHSM, the rotor dimensions of the AMEBA machine are highly restricted by the excessive air-friction loss and the critical bending frequency (CBF). For example, the air-friction loss (P_f) increases with the rotor diameter (D) as $P_f \propto D^4$ and the rotor CBF ($\omega_{n,CBF}$) decreases with the axial length (L) as ($\omega_{n,CBF} \propto \sqrt{1/L^4}$) [10], [11]. The excessive air-friction loss reduces the machine efficiency and affects the rotor temperature distribution. On the other hand, the rotor CBF limits the AMEBA's communication bandwidth significantly. To avoid these phenomena, the magnetic loading of the AMEBA rotor cannot be increased after a certain value. In this condition, the only remaining option to increase the shaft power of the UHS AMEBA machine is to increase the stator's electrical loading.

Increasing the stator's electric loading of UHSM using the conventional three-phase winding presents several disadvantages such as larger footprint, lower power density, lower efficiency, higher back-EMF, higher axial temperature variation, which are highly undesirable in the AMEBA application. As a solution to this problem, a multi-phase winding configuration can be adopted in UHSM to increase the shaft power. It will increase the stator's electric loading with lower back-EMF and torque pulsation [12]. In addition, its inherent benefit of lower per phase input current will reduce the air-gap coil area and improve the electromagnetic

coupling between the rotor and slot-less stator, resulting in high power density and high efficiency of the UHSM.

Therefore, with these advantages, the multi-phase winding can be a better substitute compared to the three-phase winding of UHSM in the AMEBA application. However, the multi-phase winding adoption in UHSM and its comparison with the three-phase winding system has not been studied in any literature yet, to the best of the authors' knowledge. In this paper, the comparison of three-phase and six-phase UHSM is presented in terms of their design and performance characteristics.

II. UHS AMEBA Motor Geometry

The UHSMs over 100 000 r/min typically require a simple and robust design geometry to sustain at the UHS rotation. Fig. 2. shows the geometry of the studied AMEBA motor. It has a 2-pole rotor using a cylindrical Sm_2Co_{17} magnet buried inside a retaining sleeve. A slotless stator is used to ensure a smooth torque profile. The multi-strands magnetic Litz wire is used for stator winding to reduce the high-frequency eddy current effect.

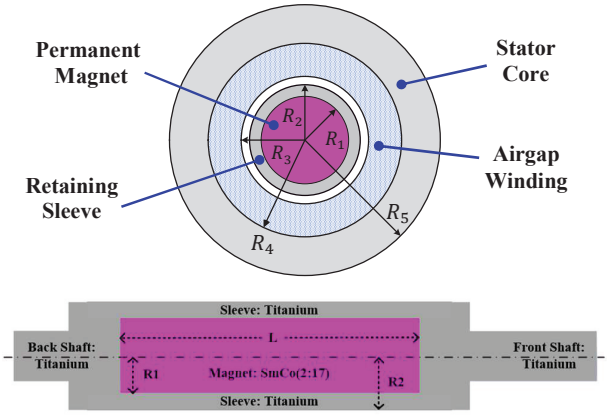

Fig. 2. Cross-section of the 2 kW, 500 000 r/min UHS machine.

One of the key requirements of the AMEBA motor is the high shaft power at UHS to drive the PPM at a faster dynamic. The output power of this motor is proportional to the magnetic loading, electrical loading, square of the air-gap diameter, the effective stack length [13], [14]. However, this UHS rotor's magnetic loading and stack length are strictly restricted by its critical mechanical aspects, such as excessive vibration and structural breakdown. Therefore, the feasible option to increase the output shaft power of a UHS AMEBA machine is to increase the electrical loading in the stator.

III. Increasing Electrical Loading in HP-UHSM

The electrical loading of a UHSM can be calculated as the total input current in the stator divided by the airgap circumference. When the air-gap is fixed, the stator electrical loading (A_s) can be expressed as (1):

$$A_S \propto \text{total ampere conductors} \propto 2mI_aN_{TP} \qquad (1)$$

where I_a is the input current, m is the number of phases, and N_{TP} is the number of turns per phase. In the UHSM, the maximum allowable electrical loading is limited by the machine's cooling capability and the maximum operating temperature. However, for a specific cooling system, increasing the electrical loading influences the machine's performance significantly.

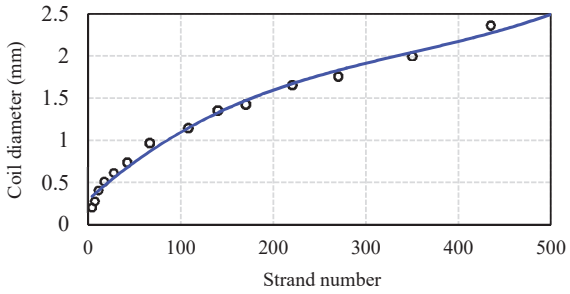

Fig. 3. Coil diameter variation with strand number generated by manufacturer's data and fitted curve [15].

TABLE I. Impact of Input Current on HP-UHSM

Phase current	Output Power	Power density	Back-EMF	Efficiency
3	1170	36	185	92.3
4	1387	32	166	91.9
5	1544	29	152	91.6
6	1727	26	141	91.2
7	1937	24	133	90.7
8	2090	22	126	90.1

TABLE II. Impact of coil trun on HP-UHSM

Turns/phase	Output Power	Power density	Back-EMF	Efficiency
20	1010	38	120	91.3
30	1308	32	155	90
40	1575	27	185	90.7
50	1806	24	213	90.2
60	2020	21	238	89.3

First, let us consider the increasing electrical loading by changing the input current. As the input current increases, the coil requires more parallel strands (N_{PS}) to withstand the supply current safely. The required strand number for a given current can be calculated as $N_{PS} = I_a/I_{cc}$, where I_{cc} is the current-carrying capacity of a single strand. Fig. 3 shows the variation of coil diameter with the strands number. One can observe that when the N_{PS} increases from 90 to 180 turns, the nominal diameter of a Litz coil (d_c) increases from 1 mm to 1.5 mm. As a result, increasing the phase current will increase the coil's required slot area and end winding length. Ultimately, it will decrease the machine's power density, calculated by $PD = P_{shaft}/\pi R_5^2 L_e$, where L_e is the effective motor length considering the end winding and R_5 is the stators outer radius as shown in Fig. 2.

Furthermore, the UHSMs use a slot-less stator to eliminate the slot harmonics. It benefits a lower core loss, lower rotor-eddy current loss, and a smooth torque profile. However, the slot-less stator results in a large effective air-gap length (distance between the PM and stator core = $R_4 - R_2$), which is inversely proportional to the electromagnetic coupling between the stator and rotor. Increasing the electrical loading by using a high input current will further increase the effective air-gap length. Consequently, the output shaft power will drop, and machine efficiency will decrease considerably.

Table-I shows the variation of UHSM performances when the input current increases. The simulated machine has a geometry similar to Fig. 2 with a three-phase winding config-

uration. The performances are simulated at 500 000 r/min, and the efficiency does not include the bearing losses. The coil diameter is changed based on the input current and manufacturer's data supplied by the company [15]. The parametric analysis shows that when the input current increases from 3 A to 8 A, the output power increases from 1170 W to 2090 W. However, the power density and efficiency of the machine are also decreased by 39% and 2.4%, respectively. The B-EMF is dropped by ~32% due to weakening the electromagnetic interaction between the stator and rotor. It also observed that the output power doesn't increase linearly with the input current. Rather, the increment becomes smaller as the input current increases.

Second, increasing the electrical loading using higher coil-turns will also decrease the machine efficiency and power density. Because the coil-turns are proportionally related to the required slot area as written in (2):

$$Slot\ Area\ (S_A) = \frac{\pi d_c^2 N_{TP}}{4 k_{SF}} + A_{insulation} \qquad (2)$$

where k_{SF} is the slot fill factor, and $A_{insulation}$ is the area of insulating material. Furthermore, higher coil-turns will considerably increase the back-electromotive force (B-EMF) especially at UHS rotation.

Table II shows the variation of a UHSM performances when the coil-turns are increased. The simulation setup is the same as the previous one, except the input current is fixed at 4 A, which means the coil diameter is fixed in this case. The N_{TP} is changed to increase the electrical loading. It is observed that the output shaft power increases from ~1 kW to ~2 kW when the number of coil-turns changes from 20 to 60. However, according to (2), as the N_{TP} increases the required slot area and end winding length also increase, which reduces the machine power density from 38 kW/L to 21 kW/L. Furthermore, it reduces the machine efficiency from 91.3% to 89.3% and increases the B-EMF from 110 V to 200 V at 500 000 r/min. Hence, the machine will require a high DC bus voltage to operate at UHS, which is not favorable for the AMEBA application considering its limited energy storage capability.

Therefore, it is concluded that the output shaft power of a UHSM can be increased by using higher coil-turns and input currents to the stator. But, these techniques reduce the machine's power density and efficiency considerably. On the other hand, the AMEBA system requires an HP-UHSM with a small footprint and high efficiency to enable bi-directional wireless communication in the RF-denied environment.

An efficient solution to this problem is to adopt a multi-phase winding in the slot-less stator to increase the input electrical loading. For a required electrical loading, increasing the phase number (m) will reduce the amplitude of per phase input current and the number of coil-turns. The former one benefits a smaller slot area by reducing the number of coil strands. It increases the power density and efficiency of the machine. The latter one results in a lower back-EMF at UHS. It reduces the required DC bus voltage and the electrical stress in the inverter leg.

IV. Multi-phase Winding in UHS AMEBA Motor

Multi-phase winding configuration in PM machine provides several inherent advantages such as high torque density, high efficiency, high fault-tolerant capability, and lower per-phase converter current rating. Considering these benefits, a multi-phase winding configuration can be a suitable candidate for the HP-UHSM to achieve the unique requirements of the AMEBA system.

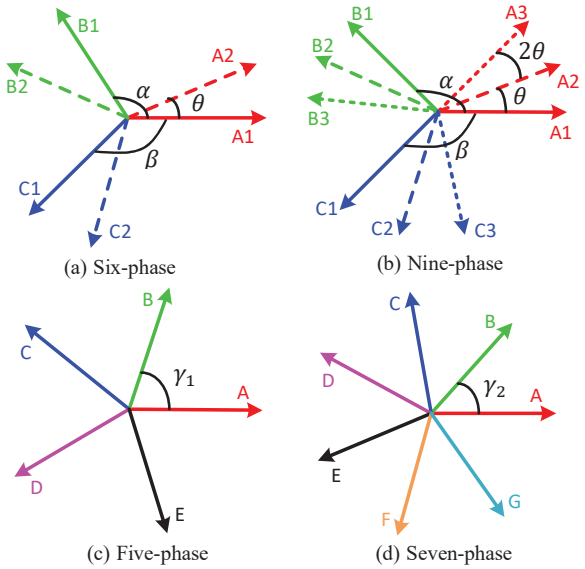

Fig. 4. Phase diagram of commonly used multi-phase winding configurations in electric machine.

In literature, extensive research has been done on multi-phase winding configuration for electric machines, especially five-phase, six-phase, seven-phase, and nine-phase [12], [16]. Fig. 4 shows the phasor diagram of commonly used multi-phase winding configurations in electrical machines. The six-phase configuration uses two sets of conventional three-phase windings: (A1-B1-C1) and (A2-B2-C2). The nine-phase configuration uses three sets of three-phase windings: (A1-B1-C1), (A2-B2-C2), and (A3-B3-C3). α is the phase shift between phase A1 and B1. β is the phase shift between phase A1 and C1. For a balanced motor system, $\alpha = \beta = 120^o$. θ is the electrical angle between the two winding sets (A1-B1-C1) and (A2-B2-C2, which can be any integer or fractional number from 0 to 360° based on the available slot number. If $\theta = 0$, then all three phase-winding sets are in phase.

The five-phase and six-phase configurations use an unconventional winding setup. All the phases are equally shifted by an electrical angle of $\gamma_1 = 360^o/5 = 72^o$ degrees for five-phase and $\gamma_2 = 360^o/7 = 51.43^o$ degrees for seven-phase configuration. These configurations offer lower electromagnetic force harmonics and higher fault-tolerant capability. However, the required electrical drive system for these configurations, such as five-phase and seven-phase inverters, is not commercially available yet. Moreover, a complex algorithm and high computational power are needed in the control system of these configurations.

On the other hand, the integer product of the three-phase system, i.e., six-phase and nine-phase configurations, can be driven by utilizing two or three commercially available conventional inverters. Therefore, these configurations are more attractive over the five-phase and seven-phase configurations. The variation of key performances of a UHSM with the three-phase, six-phase, and nine-phase

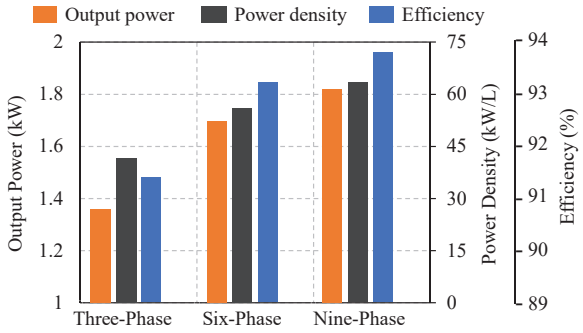

Fig. 5. Variation of UHSM performance at different multi-phase winding configurations.

winding are studied, and results are shown in Fig. 5. The machine has a geometry similar to Fig. 2, and the rated speed is 500 000 r/min. A constant current density is considered for all designs, and both the rotor and stator dimensions are fixed. The sizing variables are the input current, coil diameter, number of turns, and phase numbers.

One can observe that the maximum output power is 1350 W in the three-phase design, whereas it is increased to 1695 W in the six-phase design and 1835 W in the nine-phase design. Similarly, both the power density and efficiency are also increased as the number of phase increases. However, the output power is not increasing at the same rate as the number of phase increases. The increment is 345 W from three-phase to six-phase, whereas it is only 140 W from six-phase to nine-phase. The reasons are the higher number of slots, more coil insulations, and smaller slot area of the nine-phase design. Moreover, considering the compact design of UHSM, installing a nine-phase winding configuration in the slotless stator will be very difficult. Therefore, the six-phase configuration is considered as the optimal multi-phase winding for the HP-UHSM for AMEBA application.

V. Optimal Design Procedure of Three-Phase and Six-Phase HP-UHSM

The design of HP-UHSM is a highly iterative process when its multi-physics performances are considered [9], [17]. Furthermore, simultaneously achieving the high efficiency and high DSM of the AMEBA machine is extremely challenging due to the mutual influence of its multi-disciplinary constraints. In this study, the optimal design of a three-phase and six-phase UHS AMEBA machine is obtained by using a multi-physics design model, shown in Fig. 6. First, the machine specifications are derived from the AMEBA application requirements, such as 2-kW rated power at 500 000 r/min, >94% efficiency, >60 kW/L power density, > 30% DSM, and CBF below the fundamental operating frequency (8333 Hz). Second, the basic machine topology, active materials, and initial considerations are selected based on the required power/speed profile. Several multi-disciplinary design constraints associated with the motor topology, material limitation, and the AMEBA communication system are considered. The maximum current density limit is set to 5 A/mm^2, considering the natural air-cooling system in the machine. Then, the machine sizing is performed using a co-simulation-based multi-physics optimization which integrates the electromagnetic, thermal, mechanical, Rotordynamic, and harmonic analysis. Finally, the optimal

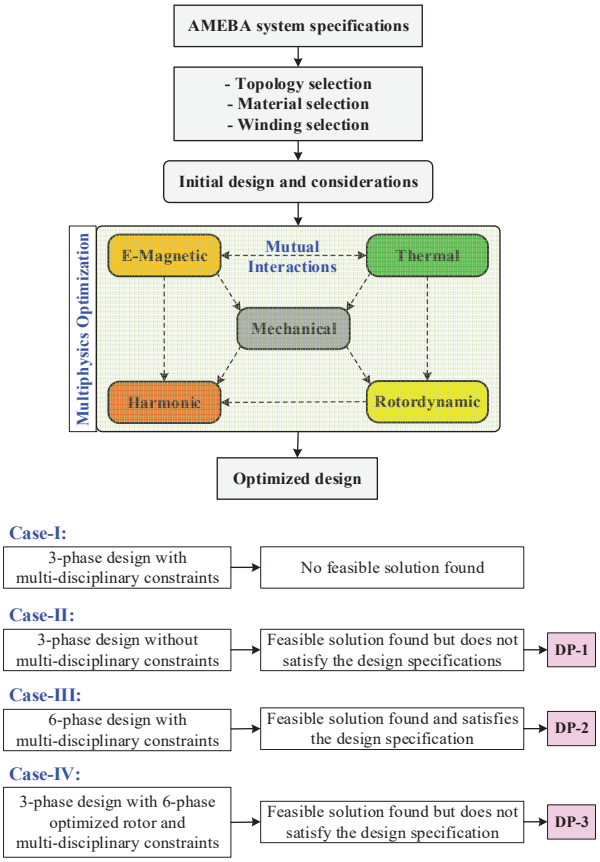

Fig. 6. Simplified multi-physics optimization process of HP-UHSM.

design point is obtained by a multi-objective algorithm. The optimal design is the one that satisfies all the specifications and provides the maximum DSM at the rated operation. In this paper, the optimization process is divided into four cases.

In case I, an attempt is taken to design the required HP-UHSM using a three-phase winding. All the multi-physics constraints are applied, such as the thermal limit, vibration limit, stress limit, and CBF limit. In this case, no feasible design point (DP) is found that satisfies the requirements, especially the rated power and power density.

In case II, the machine is again optimized using the three-phase winding, but the thermo-structural and power density constraints are ignored. In this case, a feasible solution is obtained which satisfies the electromagnetic specification only. This design point is referred to as DP-1. The design parameters are: R_1 = 4.1 mm, R_2 = 4.9 mm, R_3 = 5.6 mm, R_4 = 15.2 mm, R_5 = 17.7 mm, L = 40.2 mm, I_a = *4.5* A, N_{TP} = 30, and N_{PS} = 175.

In case III, the machine is optimized using the six-phase winding with all the multi-disciplinary constraints. For the six-phase winding, a 30 °C displacement angle is considered between the two sets of three-phase winding. In this case, several feasible DPs are found, and the optimal DP is selected from the trade-off analysis between the efficiency and the DSM. It is observed that the magnet radius (R_1) has a significant impact on the DSM and other machine performances. This design point is referred to as DP-2. The design parameters are: R_1 = 3.9 mm, R_2 = 4.6 mm, R_3 = 5.2 mm, R_4 = 11.25 mm, R_5 = 14 mm, L = 40 mm, I_a = 3.9 A, N_{TP} = 20, N_{PS} = 100.

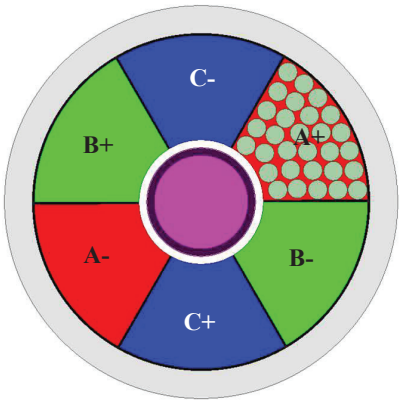

Fig. 7. 2-D geometry of DP-1 (three-phase winding).

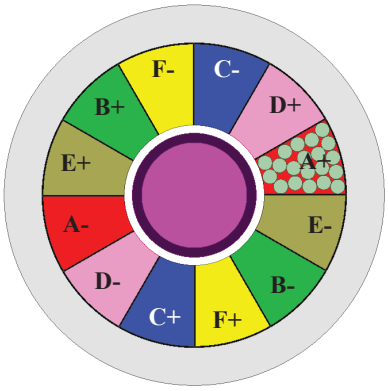

Fig. 8. 2-D geometry of DP-2 (six-phase winding).

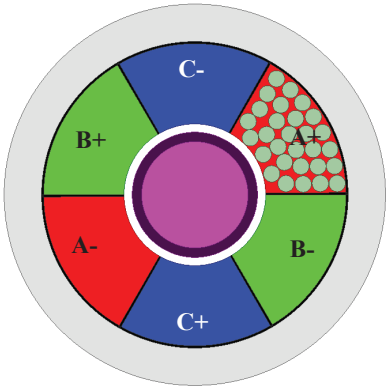

Fig. 9. 2-D geometry of DP-3 (three-phase winding in DP-2 geometry).

In case IV, a three-phase winding configuration is applied in DP-2 by keeping the same geometry parameters to compare the benefit of the six-phase winding over the three-phase winding. The value N_{TP} and I_a are optimized by maintaining the same current density of DP-2. This design is referred to as DP-3. The design parameters are: R_1 = 3.9 mm, R_2 = 4.6 mm, R_3 = 5.2 mm, R_4 = 11.25 mm, R_5 = 14 mm, L = 40 mm, I_a = 4.9 A, N_{TP} = 29, N_{PS} = 125. The geometry of these three models is shown in Fig. 7 to Fig. 9.

VI. Simulation Results

This section presents a thorough comparison of the FEA simulation results among these three design models in terms of their performance characteristics, such as back-EMF, input current, power density, electromagnetic torque, efficiency map, temperature distribution, and mechanical stress. For a fair comparison, the same materials are used in all models, and the axial rotor length is limited to 40 mm to avoid any CBF below the 8.5 kHz. The machine is operated at the rated speed of 500 000 r/min.

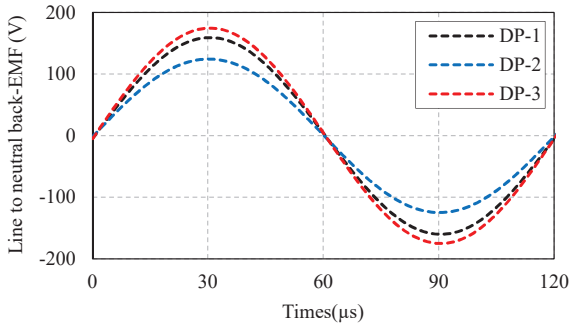

Fig. 10. Back-EMF (Phase-A) at 500 000 r/min of three design models.

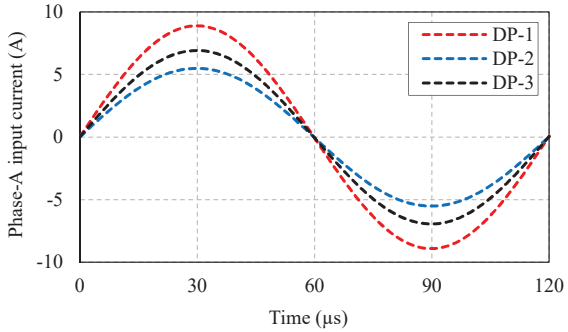

Fig. 11. Optimized input current (Phase-A) of three design models.

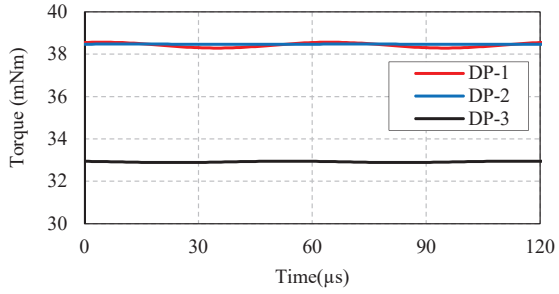

Fig. 12. Electromagnetic torque at 500 000 r/min of three design models.

A. Comparison of no-load operation

The machines are simulated at 500 000 r/min in no current condition. Fig. 10 shows the line to neutral back-EMF of the three design models. With the benefit of slot-less stator and cylindrical rotor, all models have sinusoidal back-EMF. The 6-phase design DP-2 has a peak back-EMF value of 125 V, whereas it is 160 V and 175 V in the three-phase designs DP-1 and DP-3, respectively. Therefore, the voltage stress on DP-1 and DP-3 is 30% and 40% higher than DP-2.

B. Comparison of full-load operation

The full-load simulation is conducted for all models. The machine is operated at 500 000 r/min with the optimized input current shown in Fig. 11. The DP-2 has a maximum peak current of 5.5 A. The DP-1 and DP-3 draw 62% and 28%

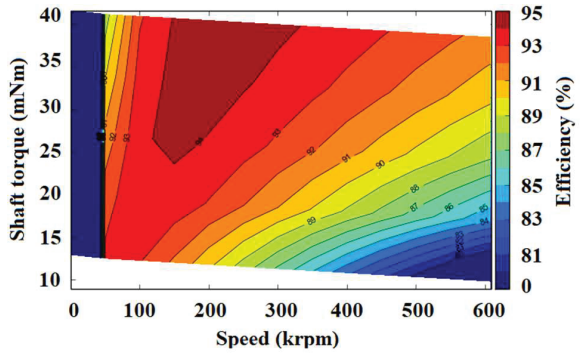

Fig. 13. Efficiency map of DP-1 obtained by 2-D FEA.

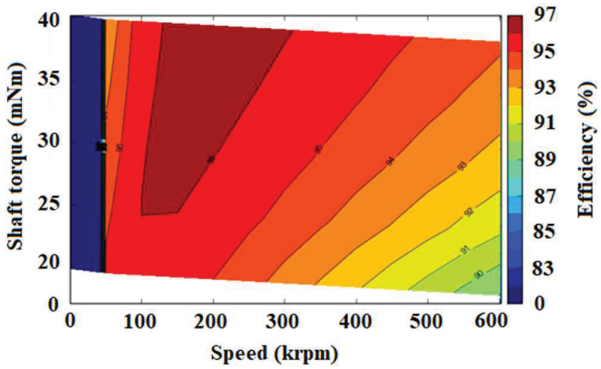

Fig. 14. Efficiency map of DP-2 obtained by 2-D FEA.

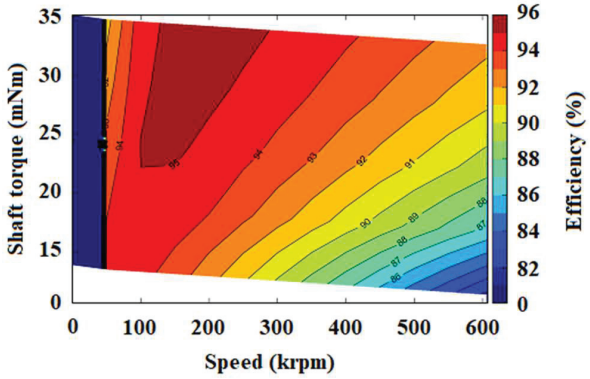

Fig. 15. Efficiency map of DP-3 obtained by 2-D FEA.

more input current than DP-2. The developed electromagnetic torques are shown in Fig. 12. The power density is calculated by $PD = P_{mechanical}/(\pi R_5^2 L_e)$. The efficiency map plot of the three models is calculated using 2-D FEA. In th efficiency calculation, the air-friction loss, stator core loss, copper loss, and rotor eddy current losses are considered, whereas the bearing loss is excluded.

It is observed that the DP-1 can provide the required output torque of 38.2 mNm, but it does not satisfy the required power density, efficiency, and DSM constraints. The outer stator radius is 17.7 mm, which does not meet the specification of the studied AMEBA system. On the other hand, the six-phase (DP-2) design develops 38.2 mNm electromagnetic torque at 500 000 r/min with a 39% lower input phase current. It has a rated efficiency of 94.5% and satisfies the AMEBA system's speed/power specifications. However, with the same machine geometry, the three-phase

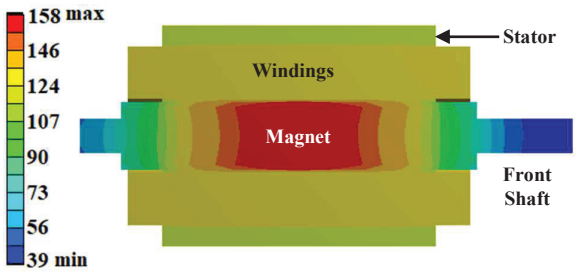

Fig. 16. Temperature distribution of DP-1 obtained by 3-D FEA (deg-C).

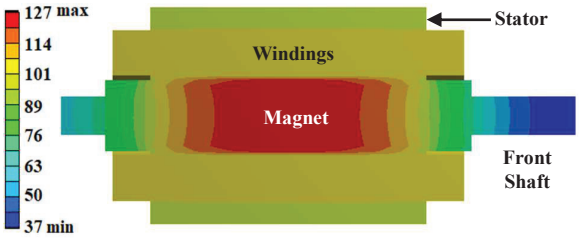

Fig. 17. Temperature distribution of DP-1 obtained by 3-D FEA (deg-C).

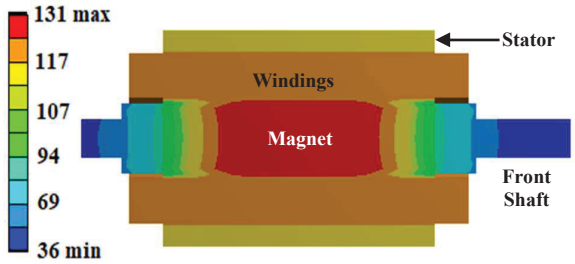

Fig. 18. Temperature distribution of DP-3 obtained by 3-D FEA (deg-C).

winding (DP-3) can generate only 32.9 mNm torque at 500 000 r/min (1720 W) with a maximum efficiency of 93.4%.

The DP-2 has a power density of 64.9 kW/L, which meets the studied AMEBA system's footprint requirement (>60 kW/L). However, the power density drops to 40.6 kW/L in the DP-1 due to a higher slot area requirement. Similarly, despite having the same geometry as DP-2, the DP-3 has a power density of 55 kW/L, 15% less than the DP-2. It is because the DP-3 generates 14% less output power than the DP-2.

C. Comparison of thermal performances.

In the AMEBA application, the machine temperature is crucial due to the limited cooling system of portable antennas. In the studied HP-UHSM machine, the operating temperature is mainly dictated by the air-frictional losses. A 3-D steady-state thermal analysis is performed to obtain the temperature distribution of the three design models. The electromagnetic and air-frictional losses are calculated from Maxwell 2-D analysis and mapped into the corresponding parts of the 3-D thermal model. The heat transfer coefficients are calculated using analytical equations of UHS machinery [18]. The radiation heat transfer were minimal and hence ignored. The thermal distribution of all models is shown in Fig. 16 to 18.

Maximum temperature is found at the magnet due to the dominant air-frictional loss on the rotor surface. Note that the temperature distribution in the magnet is not constant. Rather

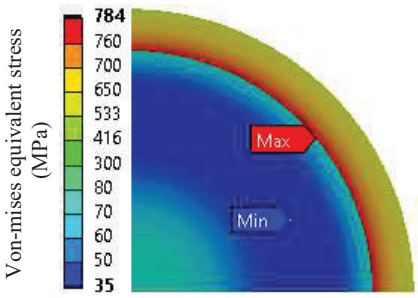

Fig. 19. Stress distribution on the rotor (DP-2) at 500 000 r/min.

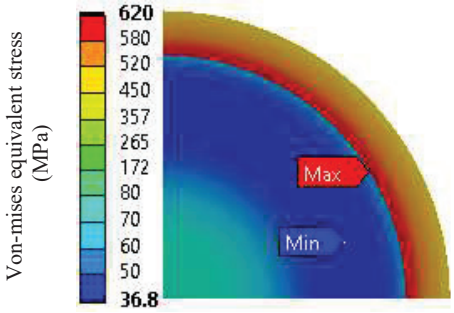

Fig. 20. Stress distribution on the rotor (DP-2) at 500 000 r/min.

it is an uneven distribution along the axial direction and the maximum temperature was found at the center of the magnet. At the rated operation, the maximum magnet temperature is 158 ºC, 127 ºC, and 131 ºC in the DP-1, DP-2, and DP-3, respectively. The variation of magnet temperature along the axial direction is 68 ºC, 18 ºC, and 38 ºC in DP-1, DP-2, and DP-3, respectively.

Due to the natural air-cooling system, the coil operating temperature is limited to 120 ºC (insulation class-F) in the AMEBA motor. The coil temperature is influenced by copper loss, air-friction loss, and stator loss. Both the AC and DC losses of the copper are considered. The maximum coil temperature is 142 ºC, 108 ºC, and 128 ºC in the DP-1, DP-2, DP-3, respectively. Therefore, the six-phase design provides a higher thermal safety compared to the three-phase designs due to the lower air-friction loss and copper loss.

D. Comparison of mechanical performances

A key limiting factor of UHSM is the structural stress developed on the rotor at ultra-high-speed rotation. In this study, DP-2 and DP-3 share the same rotor radius, but DP-1 has a higher magnet radius (R1). A 2-D FEA simulation is performed using ANSYS structural analysis to evaluate the stress distribution of the rotor. The von-mises stress is considered to calculate the stress of the rotor. Fig. 19 and Fig. 20 show the stress analysis results of DP-1 and DP-2.

It is observed that to maintain a minimum 30% stress margin in the magnet, the developed stress on the sleeve is 620 MPa in DP-2, which is 784 MPa in DP-1. Consequently, the DP-2 has a DSM of 31%, and DP-1 has a DSM of 13% only. The DSM is calculated as the developed stress on a rotor material divided by the tensile strength limit of that material. The insufficient DSM of DP-1 may lead the AMEBA rotor to mechanical breakdown and unwanted vibration. In the UHS machinery, at least 30% DSM is highly recommended to ensure a stable and safe rotation at UHS rotation.

(a) amorphous Core (b) Six-phase stator (c) Three-phase stator

Fig. 21. Stator protptype of DP-2 and DP-3 using toroidal winding.

Fig. 22. Different parts and assembly of the optimized rotor (DP-2).

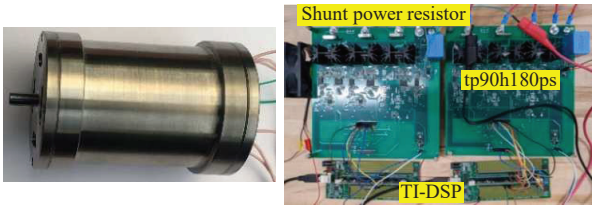

Fig. 23. (Left) full motor prototype, and (Right) customized Gan-FET based Interter.

VII. Prototyping and Experimental Results

The three-phase (DP-3) and six-phase model (DP-2) are prototyped to validate the FEA simulation results. Fig. 21 shows the slot-less stator made by the Amorphous Metglas (2605SA1) core. The Litz wire is used on the insulated core in a toroidal fashion to develop the six-phase and three-phase stator. The three-phase stator has 29 turns in each phase. Each turn consists of 125 strands of 40 AWG magnet wire, and it has a diameter of 1.17 mm. The coil is served using Poly-Nylon insulation (Class-F) to withstand the phase voltage. The six-phase stator has an asymmetric (30-degree displacement between two three-phase winding sets) winding of 20 turns. Each turn consists of 100 strands of 40 AWG magnet coil, with a diameter of 1.06 mm. The rotor has a cylindrical Sm_2Co_{17} magnet, a sleeve, and two shaft parts made of titanium alloy. The rotor is assembled using the shrink-fit technique. Fig. 22 shows the rotor parts and the assembled rotor. Fig. 23 (L) shows the full motor prototype installed in an aluminum casing using a pair or UHS bearing. A sensor-less sliding mode speed control algorithm is developed to drive the motors for the AMEBA application. A customized GaN-FET based inverter is used to reduce the switching losses. Fig. 23 (R) shows the power electronics, which is derived by the TI-DSP F28335 module.

The back-EMF of both prototypes are measured using a motor-generator cascaded operation. Fig. 24 shows the back-EMF testing result of both machines at 50 000 r/min. The back-EMF of both models are sinusoidal. The maximum phase to neutral voltage of the six-phase design is 12.5 V, whereas it is ~17.5 V in the three-phase design. Fig. 25 shows

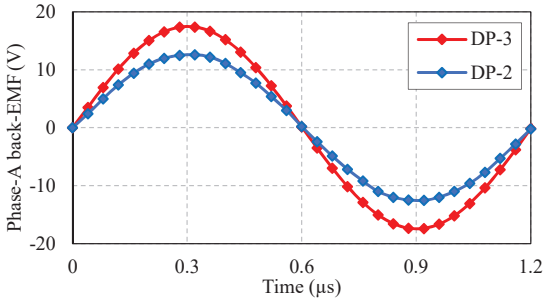

Fig. 24. Measured back-EMF of both prototypes at 500 000 r/min.

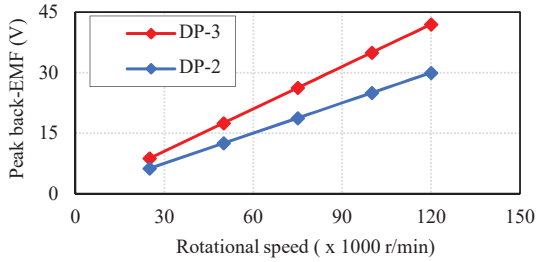

Fig. 25. Measured back-EMF vs speed variation of both prototypes.

TABLE III. MEASURED RESULTS OF REACTION TORQUE

Quantities	Six-phase			Three-phase		
RMS Phase current (A)	0.5	1.5	3	0.5	2	4
Calculated torque (mNm)	4.9	14.7	29.4	3.36	13.43	26.9
Measured torque (mNm)	4.94	14.75	29.43	3.37	13.45	26.85

the variation of the back-EMF of both machines at different speeds. The back-EMF constant of the three-phase and six-phase design is measured as 2.5×10-4 V/(r/min) and 3.5×10-4 V/(r/min), respectively. These values are closely matched with the FEA results of Fig. 10.

The torque constants of both machines are measured using the external variable resistor method. Table-III shows the torque constant results of both machines at a low speed. The six-phase and three-phase models have a torque constant of ~9.8 mNm/A and ~6.7 mNm/A, respectively. The experimental results show great agreement with the FEA results of Fig. 11 and Fig. 12.

VIII. CONCLUSION

This paper presents the comparison of optimized three-phase and six-phase UHSM with the same volume. Both models are optimized considering some unique AMEBA system requirements such as high shaft torque at 500 000 r/min, no CBF, and high efficiency with 30% multi-physics DSM. The comparative FEA result shows that the six-phase UHSM can generate 16.3% higher shaft power than its three-phase counterpart and satisfy all constraints associated with the critical AMEBA system. The six-phase model also has a 1.1% higher efficiency, 25% higher power density, 17% higher design safety margin, and 28.5% lower back-EMF. Both prototypes are built, and experimental testing is performed to validate the FEA result. The measured back-EMF is sinusoidal, and the developed torque is smooth for both models. The six-phase has a 46% higher torque constant and 28.5% lower back-EMF constant. Therefore, with the same volume, the six-phase UHSM has better electromagnetic performance and design safety margin compared with the three-phase UHSM. The other emerging applications of UHSM, where the high shaft-power, portability, and safety are important factors, the six-phase UHSM can be a better candidate over its counterpart three-phase design. Detailed experimental results such as loss analysis, full load operation, and UHS operation will be investigated in future work. Finally, the six-phase UHSM will be applied in the AMEBA communication system.

ACKNOWLEDGEMENT

This research was supported in part by the National Science Foundation CCSS-Comms Circuits & Sens System Program (Award Number 1905434).

REFERENCES

[1] D. Gerada, A. Mebarki, N. L. Brown, C. Gerada, A. Cavagnino and A. Boglietti, "High-Speed Electrical Machines: Technologies, Trends, and Developments," in IEEE Transactions on Industrial Electronics, vol. 61, no. 6, pp. 2946-2959, June 2014.

[2] Z. Huang and J. Fang, "Multiphysics Design and Optimization of High Speed Permanent-Magnet Electrical Machines for Air Blower Applications," in IEEE Transactions on Industrial Electronics, vol. 63, no. 5, pp. 2766-2774, May 2016,

[3] P. Pfister and Y. Perriard, "Very-High-Speed Slotless Permanent-Magnet Motors: Analytical Modeling, Optimization, Design, and Torque Measurement Methods," in IEEE Transactions on Industrial Electronics, vol. 57, no. 1, pp. 296-303, Jan. 2010,

[4] J. S. Glickstein, J. Liang, S. Choi, A. Madanayake and S. Mandal, "Power-Efficient ELF Wireless Communications Using Electro-Mechanical Transmitters," in *IEEE Access*, vol. 8, pp. 2455-2471, 2020.

[5] S. Gong, Y. Liu, and Y. Liu, "A Rotating-Magnet Based Mechanical Antenna (RMBMA) for ELF-ULF Wireless Communication," *Progress In Electromagnetics Research M*, Vol. 72, 125-133, 2018.

[6] J. S. Glickstein, J. Liang, S. Choi, A. Madanayake and S. Mandal, "Power-Efficient ELF Wireless Communications Using Electro-Mechanical Transmitters," *IEEE Access*, vol. 8, pp. 2455-2471, 2020.

[7] C. Zwyssig, J. Kolar, W. Thaler and M. Vohrer, "Design of a 100 W 500000 rpm permanent-magnet generator for mesoscale gas turbines", *Fourtieth IAS Annual Meeting. Conference Record of the 2005 Industry Applications Conference 2005*, pp. 253-260, 2005.

[8] C. Gong, S. Li and T. Habetler, "High-Strength Rotor Design for Ultra-High Speed Switched Reluctance Machines," in IEEE Transactions on Industry Applications, vol. 56, no. 2, pp. 1432-1442, March-April 2020.

[9] A. Borisavljevic, H. Polinder and J. A. Ferreira, "On the Speed Limits of Permanent-Magnet Machines," in *IEEE Trans. on Ind. Electron.*, vol. 57, no. 1, pp. 220-227, Jan. 2010,

[10] M. K. Islam and S. Choi, "Rotordynamic Analysis of 500 000 r/min 2 kW Ultra-High-Speed Machine for Portable Mechanical Antenna," *2021 IEEE International Electric Machines & Drives Conference (IEMDC)*, 2021, pp. 1-7.

[11] J. D. Ede, Z. Q. Zhu and D. Howe, "Rotor resonances of high-speed permanent-magnet brushless machines," in IEEE Transactions on Industry Applications, vol. 38, no. 6, pp. 1542-1548, Nov.-Dec. 2002.

[12] S. S. R. Bonthu, S. Choi and J. Baek, "Comparisons of three-phase and five-phase permanent magnet assisted synchronous reluctance motors", *IET Electr. Power Appl.*, vol. 10, no. 5, pp. 347-355, 2016.

[13] F. R. Ismagilov, N. Uzhegov, V. E. Vavilov, V. I. Bekuzin and V. V. Ayguzina, "Multidisciplinary Design of Ultra-High-Speed Electrical Machines," in IEEE Transactions on Energy Conversion, vol. 33, no. 3, pp. 1203-1212, Sept. 2018.

[14] M. K. Islam and S. Choi, "Modeling and Design of a 6-Phase Ultra-High-Speed Machine for ELF/VLF Wireless Communication Transmitter," 2021 IEEE Applied Power Electronics Conference and Exposition (APEC), 2021, pp. 1062-1069.

[15] Litz wire table. New England wire. https://www.newenglandwire.com/

[16] M. Onsal, Y. Demir and M. Aydin, "A New Nine-Phase Permanent Magnet Synchronous Motor With Consequent Pole Rotor for High-Power Traction Applications," in IEEE Transactions on Magnetics, vol. 53, no. 11, pp. 1-6, Nov. 2017, Art no. 8700606.

[17] M. K. Islam and S. Choi, "Multiphysics Optimization Model to Design High-Power Ultra-High-Speed Machine for Portable Mechanical Antenna Application," 2021 IEEE Energy Conversion Congress and Exposition (ECCE), 2021, pp. 4624-4631.

[18] C. Zhang, L. Chen, X. Wang and R. Tang, "Loss Calculation and Thermal Analysis for High-Speed Permanent Magnet Synchronous Machines," in IEEE Access, vol. 8, pp. 92627-92636, 2020.